Editors' Suggestion

Magnetic proximity beyond the interface: Layer-sequence-dependent exchange in WSe_2/CrI_3 heterostructures

Natalie Kuhn,[1] Marc Schütte,[1] Joachim Emming,[1] Felix Hellenkamp,[1] Leo Dreyer,[1] Frank Volmer,[1] Kenji Watanabe,[2] Takashi Taniguchi,[3] Lutz Waldecker,[1] Christoph Stampfer,[1,4] and Bernd Beschoten[1,*]

[1]*2nd Institute of Physics and JARA-FIT, RWTH Aachen University, 52074 Aachen, Germany*

[2]*Research Center for Electronic and Optical Materials, National Institute for Materials Science, 1-1 Namiki, Tsukuba 305-0044, Japan*

[3]*Research Center for Materials Nanoarchitectonics, National Institute for Materials Science, 1-1 Namiki, Tsukuba 305-0044, Japan*

[4]*Peter Grünberg Institute (PGI-9), Forschungszentrum Jülich, 52425 Jülich, Germany*

(Received 30 August 2026; accepted 21 October 2026; published 16 November 2026)

Magnetic proximity effects in transition metal dichalcogenide (TMD)/2D-magnet heterostructures are often described in terms of the magnetization of the interfacial magnetic layer. Here, we show that this picture is sufficient to describe the neutral-exciton valley splitting of the TMD, but incomplete for its hole-doped electronic structure. We study a gate-tunable van der Waals heterostructure composed of monolayer WSe_2 in direct contact with trilayer CrI_3. By combining spatially and helicity-resolved reflection-contrast spectroscopy with magnetic circular dichroism, we identify two distinct magnetic domains in the trilayer CrI_3: one with purely antiferromagnetic interlayer coupling and one with a mixed antiferromagnetic (AFM)/ferromagnetic (FM) coupling. In both domains, the sign of the neutral-exciton valley splitting of WSe_2 switches with the magnetization reversal of the adjacent CrI_3 layer. In contrast, helicity-resolved positive-trion spectroscopy of WSe_2 reveals a qualitatively different response. While the AFM domain shows a strongly helicity-selective trion resonance, the mixed AFM/FM domain exhibits trion resonances in both helicities. This behavior disappears when all CrI_3 layers are aligned in a parallel magnetization direction. Our results demonstrate that the positive-trion response is sensitive to the magnetic configuration of CrI_3 beyond the directly adjacent layer, revealing a magnetic proximity response that cannot be described solely by the interfacial magnetization.

DOI: 10.1103/3sgj-pdxr

I. INTRODUCTION

Van der Waals (vdW) heterostructures provide a versatile platform for proximitizing distinct two-dimensional (2D) materials and thereby tailoring their electronic, optical, and magnetic properties via interfacial proximity coupling [1–11]. A prominent example is the magnetic proximity effect in vdW heterostructures composed of monolayer transition metal dichalcogenides (TMDs) and 2D magnets, where exchange interactions induce magnetism in an otherwise nonmagnetic semiconductor [5,12–15].

Monolayer TMDs such as WSe_2 are direct-bandgap semiconductors with two energetically degenerate valleys at the K and K′ points of the Brillouin zone. At the band edge, these valley states differ not only in crystal momentum, but also in the internal orbital character of their Bloch wave functions. Together with the strong spin-orbit coupling, which ties the spin polarization to the valley index, this valley-dependent orbital structure gives rise to circular optical selection rules making the two valleys selectively addressable by circularly polarized light [16–22]. This unique coupling makes TMDs promising for spintronic [8] and valleytronic [4] applications, where the valley degree of freedom serves as an information carrier. Beyond optical excitation, an external magnetic field lifts the valley degeneracy via the valley Zeeman effect [23–26], leading to valley splittings on the order of 0.2 meV/T [23].

With the discovery of 2D magnets [27,28] and their integration into vdW heterostructures, a new route has emerged to lift the valley degeneracy in monolayer TMDs via the magnetic proximity effect [13,29]. An example is monolayer WSe_2 proximity-coupled to few-layer CrI_3 [29], where exchange interactions induce valley splittings in WSe_2 on the order of 2–3 meV [15,29–31]. Few-layer CrI_3 exhibits intralayer ferromagnetic order with an out-of-plane magnetic moment, while adjacent layers are typically coupled antiferromagnetically at zero magnetic field [see red arrows in the zoom-in of Fig. 1(a)]. Owing to the relatively weak interlayer coupling, the magnetic configuration in CrI_3 is highly tunable. An external out-of-plane magnetic field can induce layer-by-layer magnetization switching [15,27,32], while external pressure can stabilize ferromagnetic coupling even at zero

*Contact author: bernd.beschoten@physik.rwth-aachen.de

Published by the American Physical Society under the terms of the Creative Commons Attribution 4.0 International license. Further distribution of this work must maintain attribution to the author(s) and the published article's title, journal citation, and DOI.

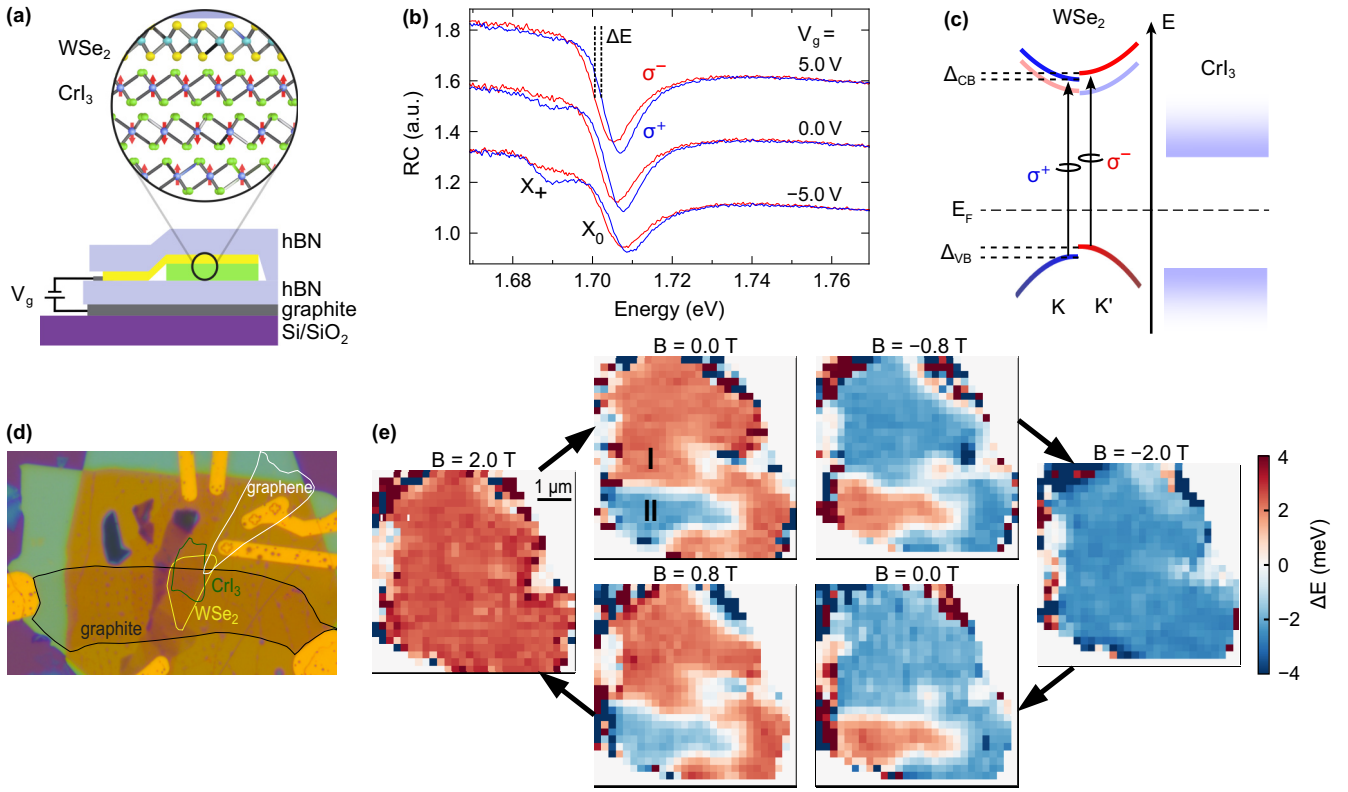


FIG. 1. Device structure and spatially resolved magnetic proximity effects. (a) Schematic cross section of a gate-tunable WSe_2/trilayer CrI_3 heterostructure, fully encapsulated in hBN. A few-layer graphite backgate and a graphene contact to WSe_2 enable electrostatic doping. (b) Helicity resolved reflection contrast at representative back gate voltages measured in region I, see panel (e). The positively charged trion (X_+) is especially prominent at negative gate voltages and vanishes at $V_g = 5$ V. The energy difference between the two light helicities of the neutral exciton (X_0) defines the proximity-induced valley splitting ΔE of the WSe_2. (c) Schematic band alignment of the WSe_2/CrI_3 heterostructure. The magnetic proximity effect lifts the valley degeneracy of WSe_2 while the staggered type II band alignment between WSe_2 and CrI_3 allows the Fermi level to be tuned into the WSe_2 valence band. (d) Optical microscope image of the device. The outlines indicate the monolayer WSe_2, trilayer CrI_3, graphite, and graphene flakes. (e) Spatial maps of the exciton valley splitting $\Delta E \approx \Delta_{CB} - \Delta_{VB}$ taken at selected magnetic fields during magnetic field down and up sweeps. At large positive and negative fields, the splitting is spatially uniform. At intermediate fields, two regions with distinct switching behavior appear: region I exhibits a single sign reversal of ΔE per sweep, whereas region II exhibits three sign reversals.

magnetic field [33,34]. Layer-resolved studies of WSe_2/CrI_3 heterostructures have shown that the sign of the proximity-induced valley splitting is predominantly determined by the magnetization of the CrI_3 layer adjacent to WSe_2. At the same time, the magnitude of the valley splitting can depend on the full magnetic configuration of the multilayer stack [15]. However, experiments have reported valley splittings with opposite signs and qualitatively distinct magnetic-field hysteresis behaviors within a single WSe_2/CrI_3 device [15,29,30]. These observations suggest that the proximity effect may not be fully captured by an interfacial picture alone and raise the open question of how the magnetic layer sequence in few-layer CrI_3 influences the proximity-induced electronic structure in adjacent TMDs.

Here, we investigate a gate-tunable WSe_2/CrI_3-heterostructure using optical reflectance spectroscopy [35]. We identify two spatially separated magnetic domains in the trilayer CrI_3 at zero magnetic field: a domain with purely antiferromagnetic interlayer coupling, hereafter referred to as the AFM domain, and a domain with mixed antiferromagnetic (AFM) and ferromagnetic (FM) interlayer coupling. By combining the proximity-induced valley splitting in WSe_2 with the magnetic circular dichroism of CrI_3 as a function of an external magnetic field, we resolve the layer-dependent magnetic configurations of the vdW heterostructure. Moreover, electrostatic gating enables hole doping of WSe_2 and the formation of positive trions. The trion resonance serves as a probe of the spin- and valley-polarized valence-band states and resident holes. We observe distinctly different trion responses in the two magnetic domains. In the AFM domain, the trion resonance appears predominantly in the helicity corresponding to the higher energy exciton resonance. In contrast, in the mixed AFM/FM domain, the trion resonance is visible in both helicities with comparable amplitudes. Once all CrI_3 layers in the mixed AFM/FM domain are switched into a parallel alignment by an external magnetic field, the trion response becomes similar to that of the AFM domain. These observations indicate that the trion response, and thus the spin- and valley-polarized valence-band states and resident holes in WSe_2, are influenced by the magnetic configuration of the CrI_3 trilayer beyond the adjacent layer. This sensitivity is qualitatively different from

that of the neutral-exciton valley splitting, whose sign follows the interfacial CrI_3 magnetization.

II. RESULTS

The device consists of a monolayer WSe_2 proximity coupled to a trilayer CrI_3 flake and fully encapsulated in hexagonal boron nitride (hBN). Both layer numbers were determined by optical contrast measurements [36,37]. A few-layer graphite flake serves as a bottom gate. Electrical contacts to WSe_2 are realized via a graphene layer. A schematic cross section and an optical image are shown in Figs. 1(a) and 1(d), respectively.

Figure 1(b) shows helicity-resolved reflection-contrast (RC) spectra recorded at gate voltages of $V_g = -5$ V, 0 V, and 5 V at a temperature of 5 K. All spectra exhibit a resonance at energies around 1.70 to 1.71 eV, which we assign to the neutral exciton X_0 in WSe_2. The energy shift between the exciton resonances, measured by the excitation and probing with either σ^+ or σ^- polarized light, stems from the proximity-induced valley splitting, which is approximately 2 meV at zero magnetic field and zero gate voltage. Toward, negative gate voltages ($V_g = -5$ V), the amplitude of the X_0 resonance is decreasing, whereas the resonance of the positively charged trion X_+ at around 1.69 eV is increasing in amplitude. The appearance of the trion X_+, which consists of an electron-hole pair bound to an additional hole from the opposite valley, indicates gate-induced hole doping of WSe_2. Notably, the trion exhibits a pronounced helicity dependence, with a significantly larger amplitude in the circular polarization corresponding to the higher energy exciton [blue lines in Fig. 1(b)], indicating that both valleys in the valence band are differently occupied. No negatively charged trion X_- is observed at any gate voltage. The presence of X_+ and the absence of X_- indicates that the Fermi level can be tuned into the valence band but not into the conduction band of WSe_2, consistent with a staggered (type II) band alignment of the heterobilayer [see Fig. 1(c)]. This band alignment is in agreement with previous reports [29] and supported by DFT/GW calculations [38]. The measured neutral-exciton valley splitting corresponds to the difference between the valley-dependent conduction- and valence-band shifts, $\Delta E \approx \Delta_{CB} - \Delta_{VB}$ [Fig. 1(c)], assuming valley-independent exciton binding energies (see Sec. IV for details about the fitting procedure and our sign convention of ΔE).

We next use the proximity-induced exciton splitting in WSe_2 as a direct measure of the valley splitting and as a local probe of the magnetic proximity effect. Using this approach, we map the spatial variation of ΔE across the heterostructure as a function of an out-of-plane magnetic field (see Sec. IV C for more details). Spatial maps of the valley-splitting taken at representative magnetic fields during the magnetic hysteresis are shown in Fig. 1(e). At ± 2 T the valley splitting is spatially uniform across the heterostructure, reaching values of approximately ± 2 meV. Upon sweeping the magnetic field from $+2$ T to 0 T, two distinct domains are seen. While most of the sample retains a positive valley splitting (red color, region I), a region in the lower-left corner (region II) exhibits a valley splitting of opposite sign (blue color). Upon further sweeping the magnetic field to -0.8 T, both regions reverse their valley splitting and at -2 T the splitting is again uniform, now with a value of approximately -2 meV (blue color). Reversing the sweep direction from -2 T to $+2$ T [lower branch in Fig. 1(e)] yields a similar overall behavior. While region I exhibits a single sign reversal of the valley splitting per sweep, region II displays three sign reversals within the same field range. The corresponding local hysteresis curves for both sweep directions are shown in Figs. 2(a) and 2(b). Since the valley splitting in WSe_2 results from the interface exchange field from CrI_3, these contrasting hysteresis behaviors indicate that the two regions experience different interfacial magnetization sequences.

A. Layer-resolved valley splitting and interlayer magnetic order

We investigate the distinct valley-splitting behavior observed in regions I and II by analyzing the magnetic-field hysteresis of the proximity-induced exciton splitting in WSe_2, together with the magnetic circular dichroism (MCD) signal of CrI_3, which probes the total magnetization of the latter (see Sec. IV for more details). The full hysteresis curves for both magnetic-field sweep directions are shown in Figs. 2(a) and 2(b) for the exciton valley splitting and in Figs. 2(e) and 2(f) for the corresponding CrI_3 MCD signal. In the following, we use the down sweep to label the magnetic-field regimes B_1–B_4 and B_1^*–B_4^* (orange curve), while the up sweep (green curve) confirms the same layer-resolved configurations with hysteretically shifted switching fields.

We first discuss region I. The MCD hysteresis curve in Fig. 2(e) exhibits four discrete MCD levels with three switchings, defining four magnetic-field regimes B_1–B_4 along the down sweep. Since the MCD signal is proportional to the total magnetization of CrI_3, these discrete MCD levels correspond to distinct magnetic configurations of the trilayer. The switching fields and overall hysteresis shape are consistent with previously reported MCD hysteresis curves of antiferromagnetically coupled CrI_3 [15,32,33]. Fig 2(a) depicts the exciton valley splitting and shows a splitting of around $+2$ meV at $B = 2.25$ T, which reverses its sign to about -2 meV during the down sweep. Notably, only a single sign reversal of the valley splitting is observed. This sign reversal coincides with the transition between the magnetic field regimes B_2 and B_3 identified in the MCD hysteresis. The up sweep shows the corresponding reversed sequence, confirming that region I maintains a purely AFM-type switching sequence for both sweep directions.

We now consider region II. The MCD hysteresis curve in Fig. 2(f) also shows four MCD levels, defining the magnetic-field regimes B_1^*–B_4^* along the down sweep. In contrast to region I, however, the switching fields associated with the highest and lowest MCD levels are significantly reduced, occurring at $B \sim 0.5$ T and -0.9 T, respectively, whereas the corresponding switching fields in the case of region I are above ± 1.5 T. Similar reductions of the magnetic switching fields have previously been reported for few-layer CrI_3 systems exhibiting mixed AFM/FM coupling, which were attributed to different stacking orders of the CrI_3 layers [33,34]. The proximity-induced valley splitting in region II, shown in Fig. 2(b), exhibits a qualitatively different behavior from that in region I. Instead of a single sign reversal, three

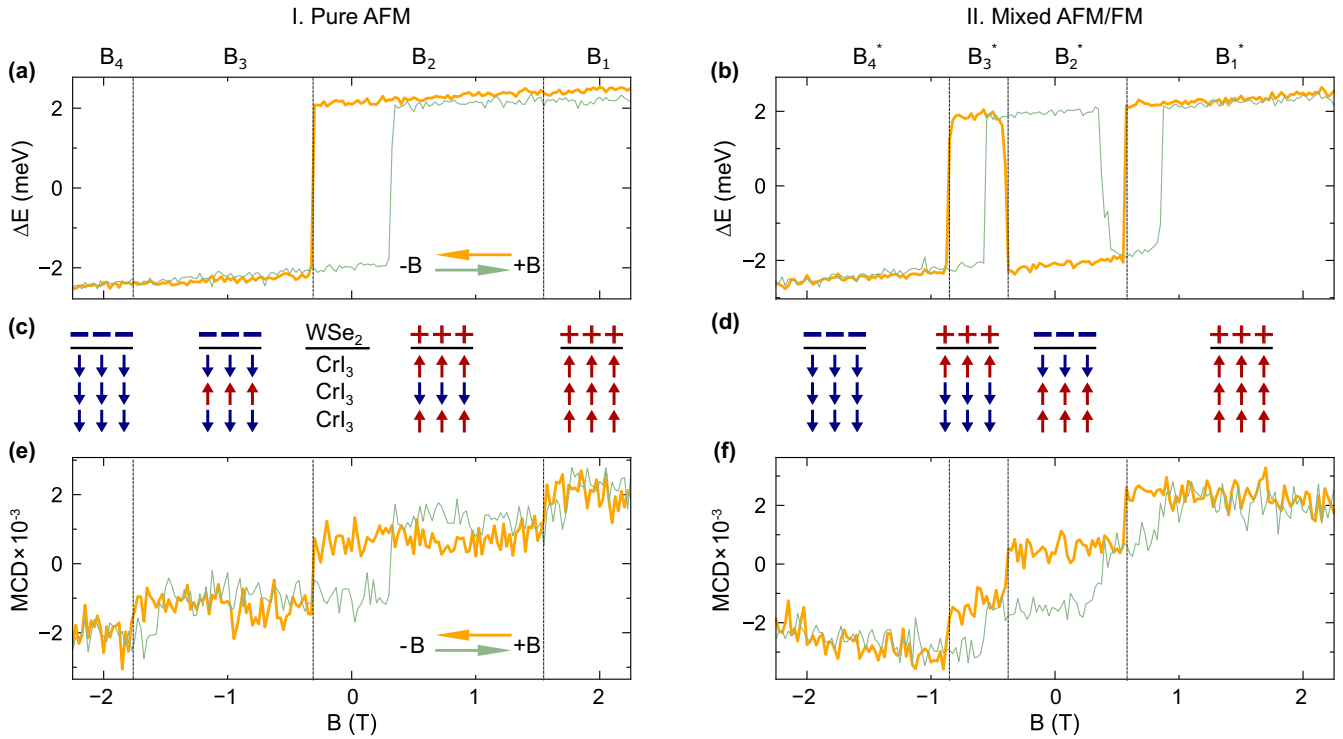


FIG. 2. Reconstruction of layer-resolved magnetic configurations. (a), (b) Magnetic field hysteresis of the proximity-induced neutral-exciton valley splitting ΔE in WSe_2 for the AFM domain (region I) and the mixed AFM/FM domain (region II), respectively. Orange and green traces correspond to the two magnetic-field sweep directions, as indicated by the arrows. Region I shows a single reversal, whereas region II shows three sign reversals. (c), (d) Reconstructed layer-resolved magnetic configurations of the heterostructure for the two regions. Plus and minus signs denote the sign of the WSe_2 valley splitting, while red upward and blue downward arrows indicate the out-of-plane magnetization direction of the individual CrI_3 layers. The configurations are labeled according to the down-sweep sequence B_1–B_4 for region I and B_1^*–B_4^* for region II; the up sweep follows the reversed sequence with hysteretically shifted switching fields. (e), (f) Magnetic circular dichroism (MCD) signal of CrI_3 for regions I and II. The MCD signal is proportional to the total CrI_3 magnetization and exhibits four discrete levels, corresponding to the net magnetizations of the magnetic trilayer. The vertical dashed lines mark the down-sweep switching fields used to define the magnetic-field regimes in (c) and (d).

sign reversals of the valley splitting are observed during the magnetic-field down sweep. Notably, the magnetic fields at which these sign reversals occur coincide with the transitions between the MCD levels in Fig. 2(f).

To identify the layer-resolved magnetic configurations underlying these observations, we use a minimal model for the CrI_3 trilayer. Each layer contributes a magnetic moment $m_i = \pm 1$ depending on the orientation of its out-of-plane magnetization. The total magnetization of the trilayer is therefore given by $M = m_1 + m_2 + m_3$, yielding $M = \pm 1, \pm 3$, consistent with the four discrete MCD levels seen in Figs. 2(e) and 2(f). While the MCD signal provides a measure of the total magnetization M, the sign of the proximity-induced valley splitting [Figs. 2(a) and 2(b)] directly reflects the magnetization of the CrI_3 layer adjacent to WSe_2 (m_1). The combination of these two observables, together with the characteristic hysteresis sequence observed in both sweep directions, allows us to infer the layer-resolved magnetic configurations. The schematics of the reconstructed layer configurations for both domains are illustrated in Figs. 2(c) and 2(d). Here, the plus and minus signs correspond to a positive and a negative valley splitting of WSe_2, respectively, while the red upward and blue downward arrows represent the out-of-plane magnetization of each individual CrI_3 layer. It is important to note that the combination of the MCD signal and the sign of the neutral-exciton valley splitting does generally not uniquely determine the magnetization direction of each CrI_3 layer. While the MCD signal provides the total magnetization and the exciton splitting predominantly reflects the interfacial magnetization, additional information from the characteristic magnetic switching sequences and the known interlayer coupling behavior is required to reconstruct the complete magnetic configurations. The assignments shown in Figs. 2(c) and 2(d) are therefore based on the combined experimental observations and the established magnetic properties of trilayer CrI_3.

In region I, the transition from B_1 ($M = +3$) to B_2 ($M = +1$) does not change the sign of the valley splitting, indicating that the interfacial layer remains polarized upward ($m_1 = +1$). Consequently, one of the remaining layers must reverse its magnetization. The observed MCD hysteresis, which matches that of antiferromagnetically coupled trilayer CrI_3, favors a configuration in which adjacent layers are antiparallel. This constraint uniquely selects the configuration to $(+1, -1, +1)$, corresponding to a reversal of the middle layer. Applying the same reasoning to the transition to B_3 ($M = -1$) yields the configuration $(-1, +1, -1)$. Finally, at large enough magnetic fields the magnetic moments of all

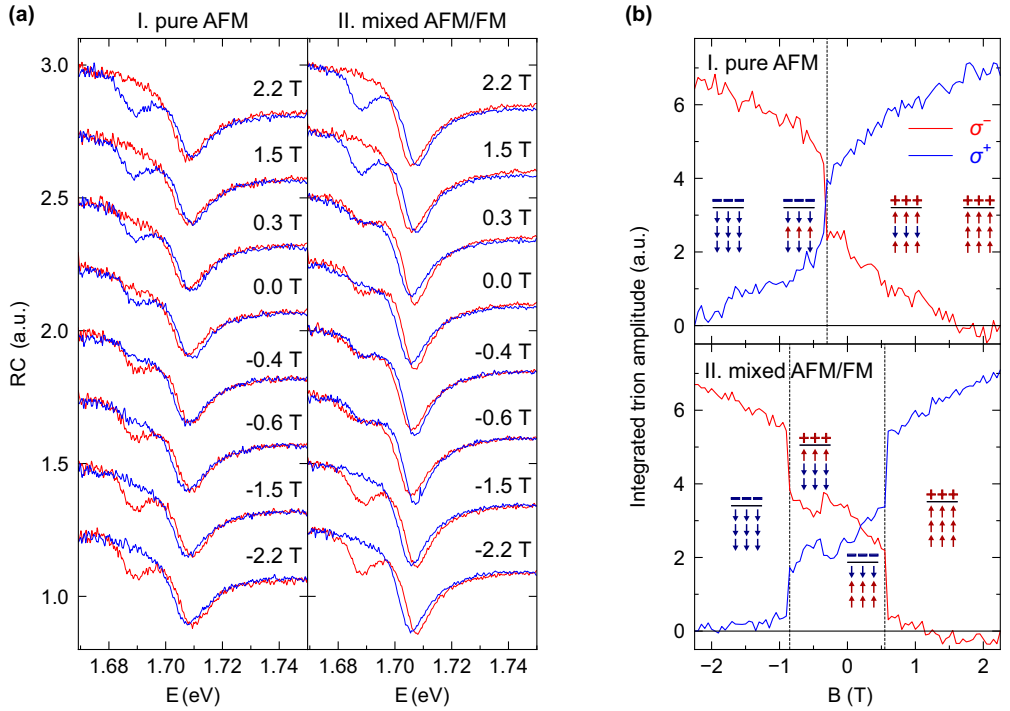


FIG. 3. Different trion response in the two distinct magnetic domains. (a) Helicity-resolved RC spectra of WSe_2 at selected magnetic fields during the magnetic field down sweep of the AFM domain and the mixed AFM/FM domain, measured at a gate voltage of $V_g = -5$ V. In the AFM domain, the positive trion X_+ is only dominant in one of the two light helicities, whereas it is almost absent in the other. The helicity, in which the feature can be observed, switches when the interfacial CrI_3 layer reverses. Instead, in the mixed domain, the trion becomes visible in both helicities in the intermediate magnetic field regime (see, e.g., curve at -0.4 T). (b) Integrated trion amplitudes for σ^+ and σ^- polarization as a function of magnetic field. In the AFM domain, the two helicities remain strongly asymmetric throughout the sweep. In the mixed AFM/FM domain, the trion amplitudes become comparable between approximately 0.5 T and -0.9 T, coinciding with the mixed magnetization sequence of the CrI_3 trilayer.

layers are aligned to the external magnetic field, yielding $(-1, -1, -1)$.

In contrast, region II exhibits a qualitatively different switching sequence. The transition from B_1^* ($M = +3$) to B_2^* ($M = +1$) is accompanied by a sign reversal of the valley splitting, indicating that the interfacial CrI_3 layer switches its magnetization. The only configuration consistent with $M = +1$ is therefore $(-1, +1, +1)$. Extending this reasoning to the subsequent transition to B_3^* ($M = -1$) leads to the configuration $(+1, -1, -1)$ and again to $(-1, -1, -1)$ at large magnetic fields in region B_4^*.

This reconstruction reveals purely AFM interlayer couplings in region I and mixed AFM/FM couplings between adjacent layers in CrI_3 in region II. Accordingly, we refer to region I as the AFM domain and to region II as the mixed AFM/FM domain. In the trilayer system, the WSe_2 serves as a probe of the interfacial CrI_3 magnetization, enabling us to determine which of the remaining layers align ferromagnetically. This provides direct access to the layer-resolved magnetic order and demonstrates the presence of a partially ferromagnetic alignment in CrI_3.

B. Trion spectroscopy of layer-resolved magnetic configurations

After reconstructing the layer-resolved magnetic configuration of the CrI_3 trilayer, we next examine whether the RC signals of trions in WSe_2 are also controlled solely by the interfacial CrI_3 layer, as it is the case for the neutral excitons in both the AFM and mixed AFM/FM domains of the heterostructure. To this end, we use the positively charged trion X_+ as a charge-sensitive optical probe for the electronic states near the valence band maximum of WSe_2. In contrast to the neutral exciton, whose energy splitting primarily tracks the proximity-induced valley splitting, the appearance of the X_+ resonance depends also on the availability of resident holes in the spin-valley-locked valence-band states. Helicity-resolved trion spectroscopy therefore provides access both to the valley-dependent hole population and to changes of the valence band alignment in the proximitized WSe_2.

Figure 3(a) shows helicity-resolved RC spectra measured at $V_g = -5$ V during the magnetic-field down sweep for the AFM and the mixed AFM/FM domains. In the AFM domain (left panel), the trion resonance is strongly helicity selective. At all magnetic fields, the trion appears predominantly in the one helicity that corresponds to the blueshifted neutral exciton resonance (blue curves for $B \geqslant 0$ T, red curves for $B \leqslant -0.4$ T). Accordingly, upon sweeping the magnetic field through the reversal of the interfacial CrI_3 layer, the dominant trion helicity switches (compare the spectra at $B = 0$ T and -0.4 T). Thus, in the AFM domain, the trion response follows the sign of the interfacial proximity exchange field during magnetization reversal.

The mixed AFM/FM domain (right panel) behaves differently. In the high magnetic field regimes ($B = \pm 2.2$ T), where all CrI_3 layers are aligned parallel, the spectra closely resemble those of the AFM domain: the trion is again seen in only the one helicity that exhibits the neutral exciton resonance at higher energy. In the intermediate magnetic field regime between 0.3 T and −0.6 T, however, where the magnetic layer sequence contains both AFM and FM interlayer coupling, the trion response changes qualitatively. The trion resonance is now visible in both light helicities with comparable but overall reduced amplitudes.

We quantify this behavior by integrating the RC signal over the trion resonance and subtract the background amplitude extracted from a spectrum taken at $B = 2.5$ T (see Sec. IV for more details). The resulting helicity-resolved amplitudes for the magnetic down-sweep direction are shown in Fig. 3(b). In the AFM domain, the two helicities show a complementary field dependence and interchange at the magnetic switching field (coercive field) of the interfacial CrI_3 layer [see dashed line in the upper panel of Fig. 3(b)]. By contrast, in the mixed AFM/FM domain between approximately −0.9 T and 0.5 T both helicities exhibit trion resonances with comparable amplitudes [see magnetic range between the two dashed lines in the lower panel of Fig. 3(b)]. This is precisely the magnetic field range with the partial FM ordering [compare to B_2^* and B_3^* in Figs. 2(b), 2(d), and 2(f)].

C. Discussion

A possible interpretation of our finding is that the mixed AFM/FM configuration modifies the valley-dependent occupation of the WSe_2 valence band. As the formation of positive trions requires resident holes, the trion oscillator strength is strongly affected by the relative occupation of the spin-valley-locked valence band states. Both in the AFM domain and at large magnetic fields also in the mixed domain, the helicity selectivity of the trion resonance indicates a large imbalance of the holes between the two valleys. However, at smaller fields in the mixed AFM/FM configuration, the appearance of X_+ in both helicities indicates a reduced valley selective hole imbalance. This may originate from a modified valence band alignment, a reduced effective valence band splitting, or changes in interlayer charge transfer. The present experiment does not allow us to separate these contributions, as the measured neutral-exciton splitting remains of comparable splitting for all configurations.

An alternative explanation could be that the two domains may differ by crystallographic stacking order [33,34,39,40]. Indeed, mixed AFM/FM interlayer coupling in CrI_3 has been linked to stacking dependent interlayer exchange. However, stacking alone cannot explain the observed full magnetic field dependence. The two domains show their strongest differences only at smaller magnetic fields, whereas the trion response becomes the same once the CrI_3 trilayer is driven into a fully parallel alignment at high fields. As the stacking order is not expected to change during the magnetic field sweep, the disappearance of the domain-dependent response at high magnetic fields indicates that the relevant control parameter is the magnetic layer sequence itself.

III. CONCLUSION

In conclusion, we have investigated magnetic proximity effects in a gate-tunable WSe_2/trilayer-CrI_3 heterostructure exhibiting two distinct magnetic domains with purely AFM and mixed AFM/FM interlayer coupling. By combining helicity-resolved reflection-contrast spectroscopy with magnetic circular dichroism, we reconstruct the layer-resolved magnetic configurations and investigate their influence on the neutral- and charged-exciton responses of WSe_2. While the sign of the neutral-exciton valley splitting predominantly follows the magnetization of the interfacial CrI_3 layer, the positive-trion response exhibits a qualitatively different sensitivity to the magnetic configuration. In particular, the mixed AFM/FM domain shows trion resonances in both optical helicities, whereas the purely AFM domain remains strongly helicity selective. This difference disappears when the CrI_3 trilayer is driven into a fully polarized state. Our results therefore refine the common picture of magnetic proximity effects in WSe_2/CrI_3 heterostructures. While the neutral exciton mainly senses the interfacial CrI_3 magnetization, the positive trion probes the hole-doped electronic structure and is sensitive to magnetic order beyond the immediate interface. Although the present measurements do not allow us to independently resolve the contributions of individual CrI_3 layers to the trion response, they demonstrate that the magnetic configuration of the multilayer stack can influence the optical properties of charged excitations in the adjacent TMD. This distinction is particularly relevant for proximity-engineered spintronic and valleytronic devices, where the relevant degrees of freedom are often resident electrons or holes rather than neutral excitons.

IV. METHODS

A. Sample preparation

All 2D materials were mechanically exfoliated from bulk crystals onto Si/SiO_2 substrates using heat-assisted exfoliation. Monolayer WSe_2 and trilayer CrI_3 were exfoliated inside a nitrogen-filled glovebox, while graphite and hBN were exfoliated under ambient conditions and subsequently transferred into the glovebox. Suitable flakes were identified using an automated flake-detection algorithm [36,37]. The heterostructure was assembled inside the glovebox using a polycarbonate-assisted dry-transfer method [41] with a droplet-shaped tool [42].

Special care was taken to minimize degradation of CrI_3, which is sensitive to oxygen, water, and UV light [43]. To reduce high-energy light exposure, long-pass filters (530 nm cut off wavelength) were installed in the used microscopes, and the glovebox was equipped with UV-blocking foil (520 nm cut off wavelength). Substrates were heated to 325 °C and subsequently cooled to 70 °C before exfoliation to reduce adsorbed water and surface contamination. The trilayer CrI_3 used in this work was encapsulated within 28 h after exfoliation. After hBN encapsulation, the heterostructure remained stable under ambient conditions. Electrical contacts were defined by electron-beam lithography. The contact regions were opened by SF_6/Ar reactive-ion etching, followed by Cr/Au metallization.

The two magnetic domains cannot intentionally be fabricated. While the CrI_3 layer number was determined before assembly, its local crystallographic stacking order was not characterized.

B. Helicity-resolved optical reflectance measurements

Optical reflectance measurements were performed in a liquid-helium bath cryostat (attoLIQUID1000, attocube systems AG) equipped with an optical head, a spectrometer, and a superconducting magnet immersed in the helium bath, allowing the application of out-of-plane magnetic fields. A tungsten-halogen white-light source is collimated and directed through a linear polarizer, followed by a liquid-crystal variable retarder, which is used to switch between σ^+ and σ^- circular polarization. The circularly polarized light is routed via a 50 : 50 beamsplitter and focused onto the sample using a $100\times$ objective, resulting in a spot diameter of approximately 0.5 μm full-width half maximum. The reflected light retraces the same optical path through the objective and the 50 : 50 beam splitter, passes an additional 90 : 10 beam splitter, and is subsequently coupled into an optical fiber connected to a spectrometer equipped with a 1200 grooves/mm grating. For each spatial map, reflected intensities are recorded sequentially using σ^+ and σ^- circular polarization. From these helicity-resolved reflectance signals, both the reflectance contrast (RC) and the magnetic circular dichroism (MCD) are extracted, as defined below.

The RC is defined as

$$\mathrm{RC}(E) = \frac{I_\mathrm{s}(E) - I_\mathrm{bg}(E)}{I_\mathrm{ref}(E) - I_\mathrm{bg}(E)},$$

where $I_\mathrm{s}(E)$ denotes the reflected intensity measured on the sample region, $I_\mathrm{ref}(E)$ the reflected intensity measured on a reference region without WSe_2, and $I_\mathrm{bg}(E)$ the background signal.

The MCD is defined as

$$\mathrm{MCD}(E) = \frac{I^+(E) - I^-(E)}{I^+(E) + I^-(E)},$$

with $I^+(E)$ and $I^-(E)$ as the reflected intensities measured with σ^+ and σ^- circular polarization, respectively. The MCD signal of CrI_3 is obtained by integrating the helicity-resolved intensities over the energy range from 1.743 eV to 1.755 eV. The resulting MCD is calculated separately for the reference and both sample regions (I and II), averaged within each region, and the reference contribution is subtracted from the signals of both samples regions.

C. Exciton energy and valley splitting determined by Fano fits

To determine the energy of the neutral exciton, we fit the helicity-resolved RC spectra with Fano resonances. The RC spectrum is modeled as the sum of two Fano resonances, describing the neutral exciton X_0 and the positively charged trion X_+, together with a constant offset,

$$F(E) = f_{X^0}(E) + f_{X^+}(E) + b_0. \tag{1}$$

Each resonance is described by

$$f(E) = \frac{A_0}{1+q^2}\frac{[\Gamma q + (E - E_0)]^2}{(E - E_0)^2 + \Gamma^2}. \tag{2}$$

Here, E_0 is the resonance energy, Γ the linewidth, A_0 the amplitude, q the Fano asymmetry parameter, and b_0 a constant background offset. The Fano parameter q is taken to be identical for the exciton and trion contributions within a given spectrum.

For each magnetic field and circular helicity, the RC spectrum is fitted independently. The fits are restricted to the spectral range containing the neutral exciton and trion resonances. The exciton valley splitting is then obtained from the difference between the fitted exciton resonance energies in σ^+ and σ^- polarization,

$$\Delta E = E_{X^0}^{\sigma^+} - E_{X^0}^{\sigma^-}. \tag{3}$$

D. Calculation of trion amplitude

The helicity-resolved trion amplitude was extracted by integrating the RC signal over a fixed spectral window covering the X_+ resonance. For both the AFM and mixed AFM/FM domain we used the energy interval

$$\Delta E_\mathrm{trion} = [1.682\,\mathrm{eV}, 1.696\,\mathrm{eV}]. \tag{4}$$

For each helicity σ and magnetic field B, we calculate the integrated RC signal

$$S^\sigma(B) = \sum_{E \in \Delta E_\mathrm{trion}} \mathrm{RC}^\sigma(B, E). \tag{5}$$

As the trion appears as a dip in the RC spectra, a decrease of S_ref^σ corresponds to an increase of the trion oscillator strength. To define a positive trion amplitude, we subtract the integrated values from a helicity and domain-specific value

$$A_\mathrm{trion}^\sigma(B) = S_\mathrm{ref}^\sigma - S_\mathrm{trion}^\sigma(B). \tag{6}$$

Here, $S_\mathrm{trion}^\sigma(B)$ was obtained from a high-field spectrum in which the trion contribution in the corresponding helicity was minimal. With this convention, a deeper trion dip yields a larger positive value of $A_\mathrm{trion}^\sigma(B)$.

ACKNOWLEDGMENTS

This work was supported by the Deutsche Forschungsgemeinschaft (DFG, German Research Foundation) 576172609 and by the Deutsche Forschungsgemeinschaft (DFG, German Research Foundation) under Germany's Excellence Strategy–Cluster of Excellence Matter and Light for Quantum Computing (ML4Q) EXC 2004/2–390534769. K.W. and T.T. acknowledge support from the JSPS KAKENHI (Grants No. 21H05233 and No. 23H02052), the CREST (JPMJCR24A5), and JST and World Premier International Research Center Initiative (WPI), MEXT, Japan.

DATA AVAILABILITY

The data supporting the findings are available in a Zenodo repository under accession code [44].

[1] A. K. Geim and I. V. Grigorieva, Van der Waals heterostructures, Nature (London) **499**, 419 (2013).

[2] M. Gmitra and J. Fabian, Graphene on transition-metal dichalcogenides: A platform for proximity spin-orbit physics and optospintronics, Phys. Rev. B **92**, 155403 (2015).

[3] Z. Wang, C. Tang, R. Sachs, Y. Barlas, and J. Shi, Proximity-induced ferromagnetism in graphene revealed by the anomalous Hall effect, Phys. Rev. Lett. **114**, 016603 (2015).

[4] J. R. Schaibley, H. Yu, G. Clark, P. Rivera, J. S. Ross, K. L. Seyler, W. Yao, and X. Xu, Valleytronics in 2D materials, Nat. Rev. Mater. **1**, 16055 (2016).

[5] C. Zhao, T. Norden, P. Zhang, P. Zhao, Y. Cheng, F. Sun, J. P. Parry, P. Taheri, J. Wang, Y. Yang, T. Scrace, K. Kang, S. Yang, G.-X. Miao, R. Sabirianov, G. Kioseoglou, W. Huang, A. Petrou, and H. Zeng, Enhanced valley splitting in monolayer WSe_2 due to magnetic exchange field, Nat. Nanotechnol. **12**, 757 (2017).

[6] G.-H. Lee and H.-J. Lee, Proximity coupling in superconductor-graphene heterostructures, Rep. Prog. Phys. **81**, 056502 (2018).

[7] K. F. Mak, J. Shan, and D. C. Ralph, Probing and controlling magnetic states in 2D layered magnetic materials, Nat. Rev. Phys. **1**, 646 (2019).

[8] J. F. Sierra, J. Fabian, R. K. Kawakami, S. Roche, and S. O. Valenzuela, Van der Waals heterostructures for spintronics and opto-spintronics, Nat. Nanotechnol. **16**, 856 (2021).

[9] E.-M. Choi, K. I. Sim, K. S. Burch, and Y. H. Lee, Emergent multifunctional magnetic proximity in van der Waals layered heterostructures, Adv. Sci. **9**, 2200186 (2022).

[10] F. Volmer, M. Ersfeld, P. E. Faria Junior, L. Waldecker, B. Parashar, L. Rathmann, S. Dubey, I. Cojocariu, V. Feyer, K. Watanabe, T. Taniguchi, C. M. Schneider, L. Plucinski, C. Stampfer, J. Fabian, and B. Beschoten, Twist angle dependent interlayer transfer of valley polarization from excitons to free charge carriers in $WSe_2/MoSe_2$ heterobilayers, npj 2D Mater. Appl. **7**, 58 (2023).

[11] K. Zollner and J. Fabian, Proximity effects, topological states, and correlated physics in graphene heterostructures, 2D Mater. **12**, 013004 (2025).

[12] T. Norden, C. Zhao, P. Zhang, R. Sabirianov, A. Petrou, and H. Zeng, Giant valley splitting in monolayer WS_2 by magnetic proximity effect, Nat. Commun. **10**, 4163 (2019).

[13] L. Ciorciaro, M. Kroner, K. Watanabe, T. Taniguchi, and A. Imamoglu, Observation of magnetic proximity effect using resonant optical spectroscopy of an electrically tunable $MoSe_2/CrBr_3$ heterostructure, Phys. Rev. Lett. **124**, 197401 (2020).

[14] K. Zollner, P. E. Faria Junior, and J. Fabian, Proximity exchange effects in $MoSe_2$ and WSe_2 heterostructures with CrI_3: Twist angle, layer, and gate dependence, Phys. Rev. B **100**, 085128 (2019).

[15] D. Zhong, K. L. Seyler, X. Linpeng, N. P. Wilson, T. Taniguchi, K. Watanabe, M. A. McGuire, K.-M. C. Fu, D. Xiao, W. Yao, and X. Xu, Layer-resolved magnetic proximity effect in van der Waals heterostructures, Nat. Nanotechnol. **15**, 187 (2020).

[16] K. F. Mak, K. He, J. Shan, and T. F. Heinz, Control of valley polarization in monolayer MoS_2 by optical helicity, Nat. Nanotechnol. **7**, 494 (2012).

[17] D. Xiao, G.-B. Liu, W. Feng, X. Xu, and W. Yao, Coupled spin and valley physics in monolayers of MoS_2, Phys. Rev. Lett. **108**, 196802 (2012).

[18] X. Xu, W. Yao, D. Xiao, and T. F. Heinz, Spin and pseudospins in layered transition metal dichalcogenides, Nat. Phys. **10**, 343 (2014).

[19] L. Yang, N. A. Sinitsyn, W. Chen, J. Yuan, J. Zhang, J. Lou, and S. A. Crooker, Long-lived nanosecond spin relaxation and spin coherence of electrons in monolayer MoS_2 and WS_2, Nat. Phys. **11**, 830 (2015).

[20] F. Volmer, S. Pissinger, M. Ersfeld, S. Kuhlen, C. Stampfer, and B. Beschoten, Intervalley dark trion states with spin lifetimes of 150 ns in WSe_2, Phys. Rev. B **95**, 235408 (2017).

[21] M. Ersfeld, F. Volmer, P. M. M. C. de Melo, R. de Winter, M. Heithoff, Z. Zanolli, C. Stampfer, M. J. Verstraete, and B. Beschoten, Spin states protected from intrinsic electron–phonon coupling reaching 100 ns lifetime at room temperature in $MoSe_2$, Nano Lett. **19**, 4083 (2019).

[22] M. Ersfeld, F. Volmer, L. Rathmann, L. Kotewitz, M. Heithoff, M. Lohmann, B. Yang, K. Watanabe, T. Taniguchi, L. Bartels, J. Shi, C. Stampfer, and B. Beschoten, Unveiling valley lifetimes of free charge carriers in monolayer WSe_2, Nano Lett. **20**, 3147 (2020).

[23] D. MacNeill, C. Heikes, K. F. Mak, Z. Anderson, A. Kormányos, V. Zólyomi, J. Park, and D. C. Ralph, Breaking of valley degeneracy by magnetic field in monolayer $MoSe_2$, Phys. Rev. Lett. **114**, 037401 (2015).

[24] A. Srivastava, M. Sidler, A. V. Allain, D. S. Lembke, A. Kis, and A. Imamoğlu, Valley Zeeman effect in elementary optical excitations of monolayer WSe_2, Nat. Phys. **11**, 141 (2015).

[25] G. Aivazian, Z. Gong, A. M. Jones, R.-L. Chu, J. Yan, D. G. Mandrus, C. Zhang, D. Cobden, W. Yao, and X. Xu, Magnetic control of valley pseudospin in monolayer WSe_2, Nat. Phys. **11**, 148 (2015).

[26] G. Wang, L. Bouet, M. M. Glazov, T. Amand, E. L. Ivchenko, E. Palleau, X. Marie, and B. Urbaszek, Magneto-optics in transition metal diselenide monolayers, 2D Mater. **2**, 034002 (2015).

[27] B. Huang, G. Clark, E. Navarro-Moratalla, D. R. Klein, R. Cheng, K. L. Seyler, D. Zhong, E. Schmidgall, M. A. McGuire, D. H. Cobden, W. Yao, D. Xiao, P. Jarillo-Herrero, and X. Xu, Layer-dependent ferromagnetism in a van der Waals crystal down to the monolayer limit, Nature (London) **546**, 270 (2017).

[28] C. Gong, L. Li, Z. Li, H. Ji, A. Stern, Y. Xia, T. Cao, W. Bao, C. Wang, Y. Wang, Z. Q. Qiu, R. J. Cava, S. G. Louie, J. Xia, and X. Zhang, Discovery of intrinsic ferromagnetism in two-dimensional van der Waals crystals, Nature (London) **546**, 265 (2017).

[29] D. Zhong, K. L. Seyler, X. Linpeng, R. Cheng, N. Sivadas, B. Huang, E. Schmidgall, T. Taniguchi, K. Watanabe, M. A. McGuire, W. Yao, D. Xiao, K.-M. C. Fu, and X. Xu, Van der Waals engineering of ferromagnetic semiconductor heterostructures for spin and valleytronics, Sci. Adv. **3**, e1603113 (2017).

[30] K. L. Seyler, D. Zhong, B. Huang, X. Linpeng, N. P. Wilson, T. Taniguchi, K. Watanabe, W. Yao, D. Xiao, M. A. McGuire, K. M. C. Fu, and X. Xu, Valley manipulation by optically tuning the magnetic proximity effect in WSe_2/CrI_3 heterostructures, Nano Lett. **18**, 3823 (2018).

[31] L. Li, S. Jiang, Z. Wang, K. Watanabe, T. Taniguchi, J. Shan, and K. F. Mak, Electrical switching of valley polarization in monolayer semiconductors, Phys. Rev. Mater. **4**, 104005 (2020).

[32] T. Song, X. Cai, M. W.-Y. Tu, X. Zhang, B. Huang, N. P. Wilson, K. L. Seyler, L. Zhu, T. Taniguchi, K. Watanabe, M. A.

McGuire, D. H. Cobden, D. Xiao, W. Yao, and X. Xu, Giant tunneling magnetoresistance in spin-filter van der Waals heterostructures, Science **360**, 1214 (2018).

[33] T. Song, Z. Fei, M. Yankowitz, Z. Lin, Q. Jiang, K. Hwangbo, Q. Zhang, B. Sun, T. Taniguchi, K. Watanabe, M. A. McGuire, D. Graf, T. Cao, J. H. Chu, D. H. Cobden, C. R. Dean, D. Xiao, and X. Xu, Switching 2D magnetic states via pressure tuning of layer stacking, Nat. Mater. **18**, 1298 (2019).

[34] T. Li, S. Jiang, N. Sivadas, Z. Wang, Y. Xu, D. Weber, J. E. Goldberger, K. Watanabe, T. Taniguchi, C. J. Fennie, K. Fai Mak, and J. Shan, Pressure-controlled interlayer magnetism in atomically thin CrI_3, Nat. Mater. **18**, 1303 (2019).

[35] D. Tebbe, M. Schütte, B. Kundu, B. Beschoten, P. K. Sahoo, and L. Waldecker, Hyperspectral photoluminescence and reflectance microscopy of 2D materials, Meas. Sci. Technol. **35**, 035501 (2024).

[36] J. L. Uslu, T. Ouaj, D. Tebbe, A. Nekrasov, J. H. Bertram, M. Schütte, K. Watanabe, T. Taniguchi, B. Beschoten, L. Waldecker, and C. Stampfer, An open-source robust machine learning platform for real-time detection and classification of 2D material flakes, Mach. Learn.: Sci. Technol. **5**, 015027 (2024).

[37] J.-L. Uslu, A. Nekrasov, A. Hermans, B. Beschoten, B. Leibe, L. Waldecker, and C. Stampfer, MaskTerial: A foundation model for automated 2D material flake detection, Digital Discovery **4**, 3744 (2025).

[38] M.-C. Heißenbüttel, T. Deilmann, P. Krüger, and M. Rohlfing, Valley-dependent interlayer excitons in magnetic WSe_2/CrI_3, Nano Lett. **21**, 5173 (2021).

[39] D. Soriano, C. Cardoso, and J. Fernández-Rossier, Interplay between interlayer exchange and stacking in CrI_3 bilayers, Solid State Commun. **299**, 113662 (2019).

[40] N. Sivadas, S. Okamoto, X. Xu, C. J. Fennie, and D. Xiao, Stacking-dependent magnetism in bilayer CrI_3, Nano Lett. **18**, 7658 (2018).

[41] F. Pizzocchero, L. Gammelgaard, B. S. Jessen, J. M. Caridad, L. Wang, J. Hone, P. Bøggild, and T. J. Booth, The hot pick-up technique for batch assembly of van der Waals heterostructures, Nat. Commun. **7**, 11894 (2016).

[42] T. Bisswanger, Z. Winter, A. Schmidt, F. Volmer, K. Watanabe, T. Taniguchi, C. Stampfer, and B. Beschoten, CVD bilayer graphene spin valves with 26 μm spin diffusion length at room temperature, Nano Lett. **22**, 4949 (2022).

[43] D. Shcherbakov, P. Stepanov, D. Weber, Y. Wang, J. Hu, Y. Zhu, K. Watanabe, T. Taniguchi, Z. Mao, W. Windl, J. Goldberger, M. Bockrath, and C. N. Lau, Raman spectroscopy, photocatalytic degradation, and stabilization of atomically thin chromium tri-iodide, Nano Lett. **18**, 4214 (2018).

[44] N. Kuhn *et al.*, Magnetic proximity beyond the interface: Layer-sequence-dependent exchange in WSe_2/CrI_3 heterostructures, Zenodo, 2026, doi:10.5281/zenodo.21821738.